Solar Phys (2007) 241: 235–249
DOI 10.1007/s11207-007-0370-z

Magnetic Stereoscopy of Coronal Loops in NOAA 8891

L. Feng · T. Wiegelmann · B. Inhester · S. Solanki · W.Q. Gan · P. Ruan

Received: 6 December 2006 / Accepted: 1 April 2007 /
Published online: 25 May 2007

Abstract The *Solar TErrestrial RElations Observatory* (STEREO) requires powerful tools for the three-dimensional (3D) reconstruction of the solar corona. Here we test such a program with data from SOHO and TRACE. By taking advantage of solar rotation, a newly developed stereoscopy tool for the reconstruction of coronal loops is applied to the solar active region NOAA 8891 observed from 1 March to 2 March 2000. The stereoscopic reconstruction is composed of three steps. First, we identify loop structures in two TRACE images observed from two vantage viewpoints approximately 17 degrees apart, which corresponds to observations made about 30 hours apart. In the second step, we extrapolate the magnetic field in the corona with the linear force-free field model from the photospheric line-of-sight SOHO/MDI data. Finally, combining the extrapolated field lines and one-dimensional loop curves from two different viewpoints, we obtain the 3D loop structures with the magnetic stereoscopy tool. We demonstrate that by including the magnetic modeling this tool is more powerful than pure geometrical stereoscopy, especially in resolving the ambiguities generated by classical stereoscopy. This work will be applied to the STEREO mission in the near future.

1. Introduction

The *Solar TErrestrial RElations Observatory* (STEREO) mission will provide the first opportunity to observe the Sun – Earth system simultaneously from two different viewpoints. Three-dimensional (3D) information of quiescent coronal structures as well as of dynamic

L. Feng (✉) · T. Wiegelmann · B. Inhester · S. Solanki · P. Ruan
Max-Planck-Institut fuer Sonnensystemforschung, Max-Planck-Str. 2, 37191 Katlenburg-Lindau, Germany
e-mail: feng@mps.mpg.de

L. Feng · W.Q. Gan
Purple Mountain Observatory, Chinese Academy of Sciences, Nanjing, China

phenomena such as coronal mass ejections (CMEs) can be inferred. To better understand the related physics, 3D reconstruction tools need to be developed. A fundamental 3D reconstruction task is to reconstruct coronal loops, the building blocks of the solar corona.

Stereoscopic reconstruction of coronal loops provides a reliable method to obtain more accurate physical parameters along the loop length (Aschwanden *et al.*, 1999). To measure the loop density, one needs the line-of-sight column depth, which is related to the orientation of the loop. Another parameter, the apparent density scale height as observed for an inclined loop, also varies with the inclination angle of the loop plane. Furthermore, accurate loop properties are needed to reproduce loop oscillations and to use them to measure coronal magnetic fields. We can see that improved accuracy through a 3D geometry is expected to test loop models. Furthermore, because of the high electric conductivity in the corona, loop-shaped emission features outline the magnetic field. Three-dimensional reconstructions of elementary loop structures are of fundamental importance for studying the associated (nonpotential) magnetic field and related electric currents.

Until STEREO data become available, all stereoscopy work must make use of the solar rotation and must be based on the assumption that the magnetic structures are stable within the time interval used for stereoscopy. Under the assumption of stationary loop structures, a triangulation method has been applied to *Skylab*/XUV data by Berton and Sakurai (1985) and to SOHO/EIT data by Portier-Fozzani and Inhester (2001). Aschwanden *et al.* (1999, 2000) generalized the concept of solar-rotation stereoscopy to dynamic stereoscopy, which allows the loop structures to evolve dynamically. They traced out individual loops from two EIT images observed one day apart and determined a circular fit to these loops. Although they allowed the fit parameters to smoothly vary in time, they did not use magnetic field information to obtain the 3D loop geometry.

For the STEREO mission, Wiegelmann and Inhester (2006) developed a tool of magnetic stereoscopy that combines pure geometrical stereoscopy with estimations of the local magnetic field orientation from different magnetic field models. Their work showed that the extrapolated field lines can help to remove the ambiguities inherent in classical stereoscopy. They applied their method only to a model active region from which they computed artificial loops as seen from two different viewpoints. In this work we apply this magnetic stereoscopy to real TRACE and SOHO/MDI data. This represents a test of the method to solar data affected by noise, instrumental artifacts, etc. In Section 2 we describe the observations and loop identification. In Section 3 we describe our magnetic field extrapolation method and how to project the corresponding field lines onto coronal images from two viewpoints. After we obtain the identified loop structures and the field lines projected onto the TRACE images, in Section 4 we apply the magnetic stereoscopy tool. The conclusion is given in the last section.

2. Observations and Loop Identification

The investigated long-lived active region NOAA 8891 was visible on the disk from 26 February 2000 to 9 March 2000. The TRACE Flare Catalog (http://hea-www.harvard.edu/trace/flare_catalog/index.html) lists no M or X class flares occurring in this active region during this time. For the stereoscopy work we concentrate here on the data observed on 1 March and 2 March when the active region was close to solar center. A first task is to identify one-dimensional (1D) curves out of the 2D EUV images. In the following we call these 1D structures "loops." Projected 3D magnetic field lines (which are 1D structures as well) are called "projected field lines." There was no flare happening in this active region during these

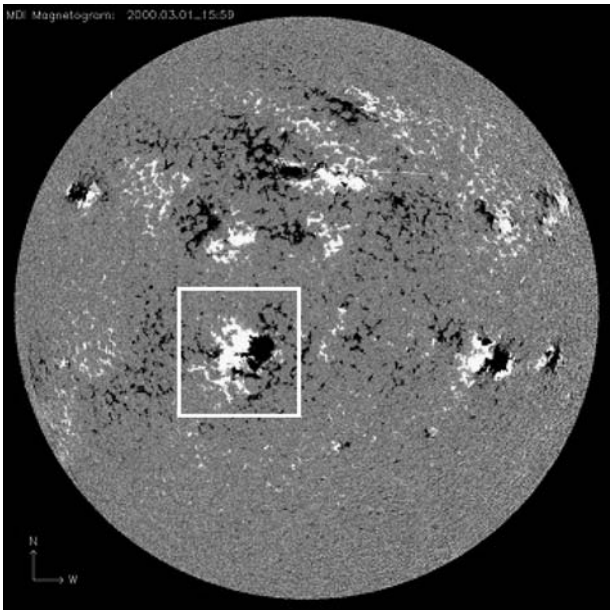

Figure 1 SOHO/MDI line-of-sight magnetogram observed on 1 March, 15:35 UT, with NOAA 8891 located in the white square.

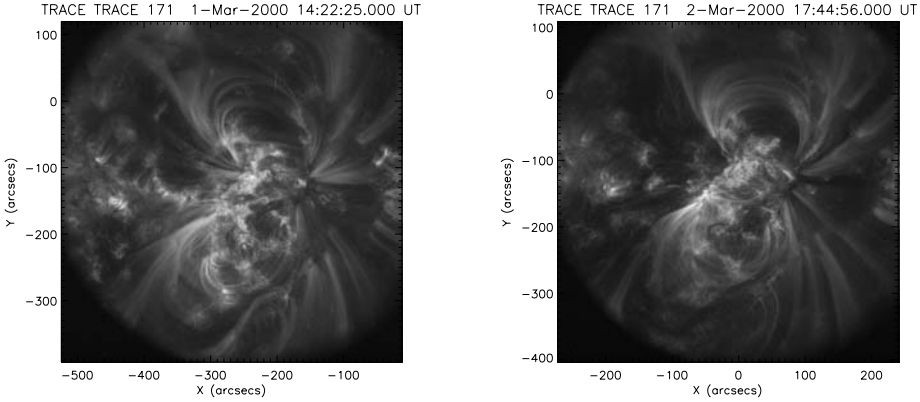

Figure 2 TRACE 171 Å data of AR 8891 on 1 March, 14:22 UT (left), and 2 March, 17:44 UT (right).

two days, so we can assume that the magnetic field was slowly evolving and can be considered as invariant over short time scales (say during one day or so). The active region we concentrate on is marked by the white square in Figure 1 observed by SOHO/MDI (Scherrer *et al.*, 1995).

Figure 2 shows two EUV images of this active region recorded by TRACE in the 171 Å waveband (Handy *et al.*, 1999) about one day apart, one on 1 March, 14:22 UT, and the other on 2 March, 17:44 UT. We can regard these two TRACE images as approximations of the EUVI image pair from the two STEREO spacecraft. To correct the TRACE pointing, the two TRACE images are calibrated separately with the SOHO/EIT (Delaboudiniere *et al.*, 1995) data closest in time (1 March, 13:00 UT, and 2 March, 19:00 UT). The sun rotated about 17 degrees during this time.

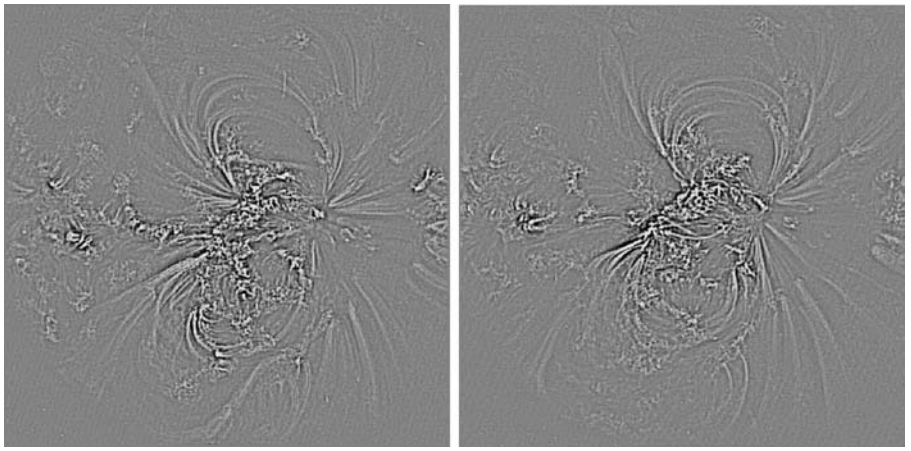

Figure 3 High-pass filtered TRACE 171 Å images on 1 March, 14:22 UT (left), and 2 March, 17:44 UT (right).

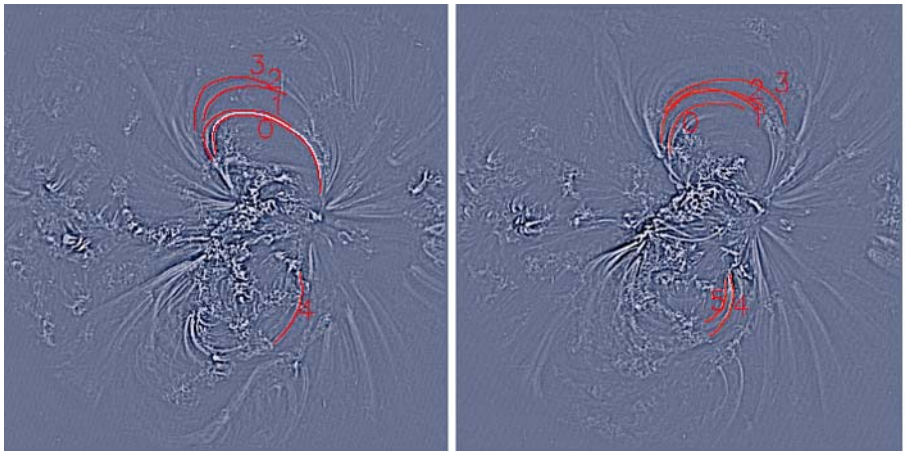

Figure 4 Hand-traced loops (red lines) marked with numbers on the filtered TRACE 171 Å images observed on 1 March, 14:22 UT (left), and 2 March, 17:44 UT (right). In the left image, the white line is segmented out from another TRACE image, which is observed on 1 March, 13:51 UT, and then transformed its coordinate onto 1 March, 14:22 UT.

Coronal loops are often visible only as faint structures, even in TRACE images, which at present have the highest spatial resolution. To enhance the loop structures in the two TRACE observations, high-pass filtered images are created by subtracting a smoothed image from the original image (see Aschwanden and Nightingale, 2005 for details). Figure 3 shows the filtered results. Subsequently, the loops are traced out in the filtered images and marked in Figure 4. Because the right part of loop 0 in the left panel of Figure 3 is invisible, a white line is shown in the left panel of Figure 4 as a reference of the direction of loop 0. It is segmented out from another TRACE image, which was observed on 1 March, 13:51 UT, about 30 min earlier. Its coordinates were then transformed onto 1 March, 14:22 UT, by aligning both images to the EIT image observed on 1 March, 13:00 UT. Loop identification is not

straightforward. Here the loops are traced by hand. Efforts toward developing an automated loop-tracing tool have been made and an overview about the current developments is given in Aschwanden (2005) and Lee, Newman, and Gary (2006).

3. Magnetic Field Extrapolation and Field Line Projection

3.1. Magnetic Field Extrapolation

The coronal magnetic field cannot usually be measured directly. Therefore one has to extrapolate it from photosphere magnetic observations (line-of-sight or vector magnetograms). Because of low β values in the lower corona, the magnetic field can be considered force-free. Let us point out that the magnetic field is not force-free in the photosphere where the field is measured. We can, however, still use the photospheric field as a boundary condition for force-free coronal magnetic field extrapolations. For nonlinear force-free extrapolations from vector magnetograms, it is necessary to preprocess the measured photospheric data in the sense of making them consistent with the assumption of a force-free magnetic field in the corona (see Wiegelmann, Inhester, and Sakurai, 2006 for details). For potential and linear force-free fields, we need only the line-of-sight photospheric magnetic field.

The required accuracy of the field lines needed to associate loops depends both on the resolution of the image and on the average distance between the individually identified loops in the image. The distance of the projected field lines to the loops should be smaller than the distance between neighboring loops.

Combined with the divergence-free condition, the force-free equations are written as

$$(\nabla \times \mathbf{B}) \times \mathbf{B} = 0; \qquad \nabla \cdot \mathbf{B} = 0; \tag{1}$$

then

$$\nabla \times \mathbf{B} = \alpha \mathbf{B}, \tag{2}$$

where α is generally a function of space (nonlinear force-free field) although often the simplification of a constant α is made (linear force-free field).

In this work, we use the method described by Seehafer (1978) to extrapolate the linear force-free field from SOHO/MDI line-of-sight magnetograms. The nonlinear force-free field model is more general and more accurate than the linear case (Wiegelmann *et al.*, 2005b), but a vector magnetogram is needed as boundary data, which is now not regularly observed. Line-of-sight magnetograms such as those provided by MDI do not provide any constraints on the electric currents. Currents are important to describe the magnetic field in active regions accurately and can to the lowest order be included with a linear force-free model. The model has one free parameter, α, which is a priori unknown. Several authors (Carcedo *et al.*, 2003; Marsch, Wiegelmann, and Xia, 2004) used coronal images in EUV, X ray, and Hα to compute the optimal linear force-free parameter α by comparing magnetic field line plots with images from a single viewpoint (*e.g.*, SOHO and *Yohkoh*).

The Seehafer solution is computed on a rectangular grid ($0 - L_x$ and $0 - L_y$) and contains the free force-free parameter α. To normalize α, we choose the harmonic mean L of L_x and L_y defined by

$$\frac{2}{L^2} = \frac{1}{L_x^2} + \frac{1}{L_y^2}. \tag{3}$$

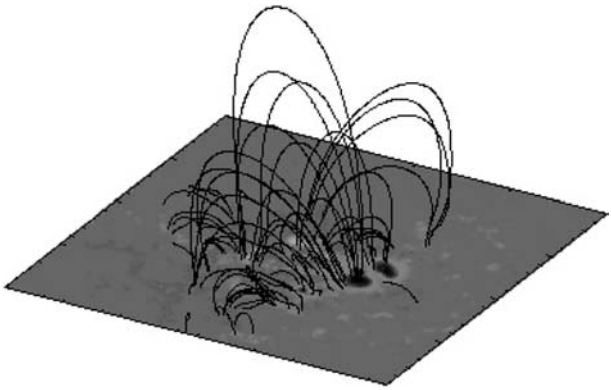

Figure 5 Three-dimensional potential magnetic field of NOAA 8891 extrapolated from SOHO/MDI data. Only closed field lines are plotted.

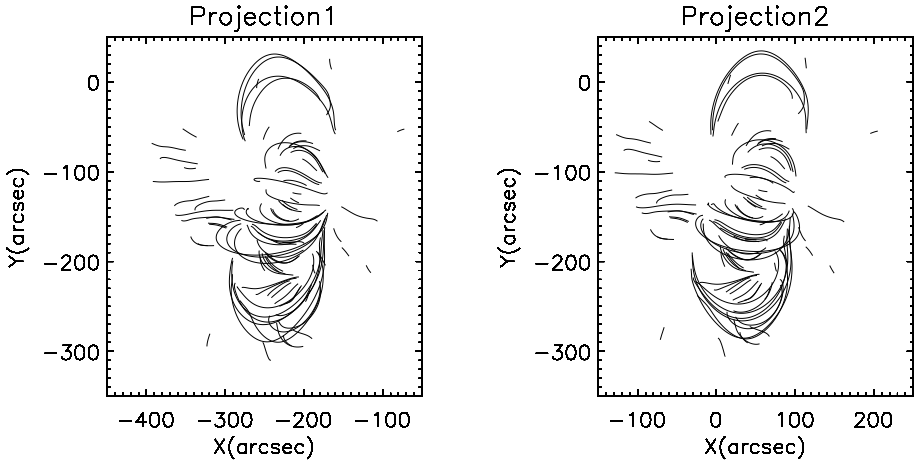

Figure 6 Projection results of the extrapolated 3D potential field lines along two TRACE view directions. The left image is for the viewpoint on 1 March, 14:22 UT, and the right one on 2 March, 17:44 UT.

The force-free parameter αL is limited by $-\sqrt{2}\pi \leq \alpha L \leq \sqrt{2}\pi$ in the Seehafer solution (see Seehafer, 1978 for details). Potential fields correspond to $\alpha = 0$.

We have computed the linear force-free field model for 45 different values of α varied from -0.0156 to 0.0156 Mm^{-1} (for convenience of calculation, the value of αL increases by 0.2 at every step). For each field line, the starting point is chosen randomly in the photosphere in the region where the magnetic field strength is larger than 20 G. In total, 4 183 field lines are stored. We show as example the potential field (*i.e.*, the case $\alpha = 0$) in Figure 5. Here only the closed field lines are plotted as we are only interested in closed coronal loops.

3.2. 3D Field Line Projection

The extrapolated 3D magnetic field lines should be projected onto both TRACE images to be compared with loop structures identified in Section 2. To facilitate the projection, we convert the position of points (x_i, y_i, z_i) on a 3D field line from the coordinate system of the extrapolation respectively to the two heliocentric coordinate systems established for the TRACE observations. (Details of the coordinate transformation are described in the

Appendix.) The projection results for the potential field lines are given in Figure 6 as an example. The left image shows the projection along the TRACE view direction on 1 March, and the right one along the view direction on the next day, 2 March. Comparing these two projection images with the two TRACE images, we can see that generally the potential field lines indicate the directions of the identified loops. A quantitative analysis will be discussed in the next section.

4. Magnetic Stereoscopy

From the analysis in Sections 2 and 3, we have five identified loop structures for one viewpoint, six loop structures for the other viewpoint, and 4 183 projected field lines for both viewpoints. They form the necessary material to reconstruct the 3D geometry of coronal loops. In a first step, we quantify the distance of the projected field lines to each loop. Two loops in different images (later we call the TRACE image observed on 1 March TRACE Image A, and the other one TRACE Image B) are defined to form a pair if there is a common field line that projects closely to both loops. Then the stereoscopic reconstruction is performed with the loop pairs found.

4.1. Loop Pair Identification

The faint, diffuse coronal plasma and the "jungle" of nested loops do not allow a clear association of loops in two TRACE images with each other. However, this is an important step before the stereoscopic reconstruction. If the problem of loop association is not solved properly, the stereoscopic reconstruction can fail or lead to incorrect results.

To quantify how good the correspondence is between a loop combination from both TRACE images, we introduce three quantities $C_{L_A L_B}(b)$, $C_{L_A}(b)$, and $C_{L_B}(b)$. $C_{L_A}(b)$ measures the average distance between the loop L_A in TRACE Image A and a certain projected

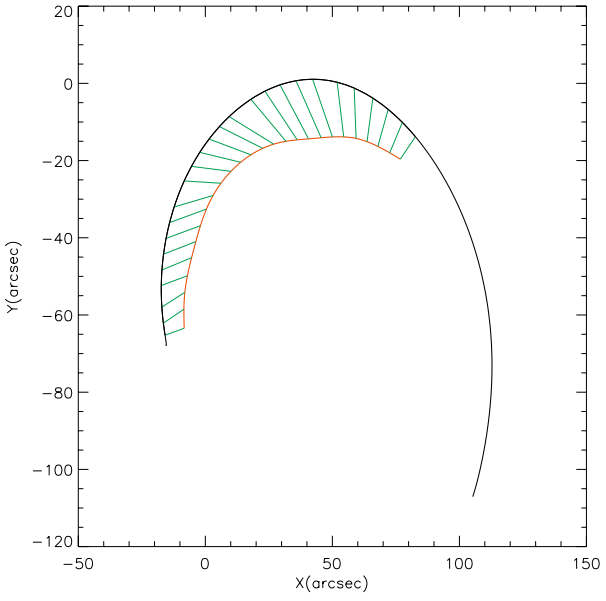

Figure 7 Plot illustrating how the parameter $C_L(b)$ is calculated. The red line is one traced loop, the black line is one projected magnetic field line, and green sticks show the area between the loop and the part of the field line corresponding to the loop.

field line b and shows how well the loop and field line agree with each other. $C_{L_B}(b)$ is similar to $C_{L_A}(b)$ but for TRACE Image B. Both are defined as the area between the traced loop and the projected field line divided by the loop length (see Figure 7). $C_{L_A L_B}(b)$ is the average of $C_{L_A}(b)$ and $C_{L_B}(b)$. Two points should be mentioned here. First, for the case that the field line is much shorter than the loop, they do for obvious reasons not match well. We penalize $C_{L_A}(b)$ or $C_{L_B}(b)$ by a large number (1 000 arcsec in our calculation). Conversely, if the observed loop is shorter than the projected field line, this match is accepted. Second, because it is difficult to trace the exact positions of the loop footpoints, the section near the footpoints of the loops is omitted to get a more precise average distance (see Figure 7 as an example).

For each loop pair combination, that is, one loop picked from Image A and the other loop picked from Image B, we can find a certain field line from the total of 4 183 field lines that minimizes $C_{L_A L_B}(b)$. It is easy to understand that the smaller $C_{L_A L_B}(b)$ is, the better the loop pair associate with each other. For a better visualization, we plot $1/C_{L_A L_B}(b)$ in Figure 8 (left), which shows the initial results of loop matching. The loop pairs found in this way and their best-fitting field lines are used later as reference to get further results.

Because the starting footpoints of all the 4 183 field lines we calculated here are randomly selected on the photosphere and the interval of the 45 α values is not small enough, we might have missed some more precise candidates that fit the loop pairs even better. To find these improved candidates, for each possible loop pair found from the initial results, we calculate additional field lines with smaller steps in α and with their footpoints focused near the footpoint of the optimal field line found so far. The starting points on the photosphere of the new field lines are regularly distributed on a 10-arcsec-wide circle centered at the starting point of the old optimal field line associated with the respective loop pair. Moreover, the αL in steps of 0.1 are varied around the value of the old optimal field line. Now comparing all the 2 585 new field lines gathered from every group with the loops traced from Image A and Image B, we obtain a more precise result (see the right panel of Figure 8). The most probable loop pair that has the smallest value of $C_{L_A L_B}(b)$ has now changed from loop pair (1-1) ($C = 3.71$ arcsec) to loop pair (0-0) ($C = 1.54$ arcsec). From Figure 8 we can see the maximum value of the vertical axis increases from 0.3 to 0.8.

All the possible loop pairs we have found are listed in Table 1 with the αL value of the field line that best fits each loop pair. The obtained fits suffer from the nonsimultaneous recording of the two TRACE images, and so the loop structures may have evolved from one day to the other owing to the lifetime of EUV loops. This problem will disappear once STEREO data become available. Table 1 demonstrates that there need not be a one-to-one correspondence between loops and field lines. Loop pairs 2 and 3 both contain loop 1 in Image A. $C_{L_A L_B}(b)$ is relatively similar in both cases, so it can only formally be used to favor loop pair 2. In view of the nonuniqueness of loop pair combinations and loop evolution, we only reconstruct the 3D loop for the most probable loop pair (0-0) in the next subsection. This loop pair and its best-fitting field line are shown in Figure 9. The correspondence is surprisingly good, considering the uncertainties inherent in magnetograph measurements (which do not compensate for the unknown properties of magnetic elements; see, *e.g.*, Solanki, 1993).

In this work we extrapolate the magnetic field with the linear force-free field model that assumes constant α value in this active region. However, from Table 1 we find negative α values for the loop pairs in the northern part of this active region, whereas in the southern part, positive α values are obtained. This is in contradiction with the linear force-free assumption and indicates that this magnetic field model is not a perfect approximation of the loops in NOAA 8891. It should be noted that the magnetic field lines that were calculated

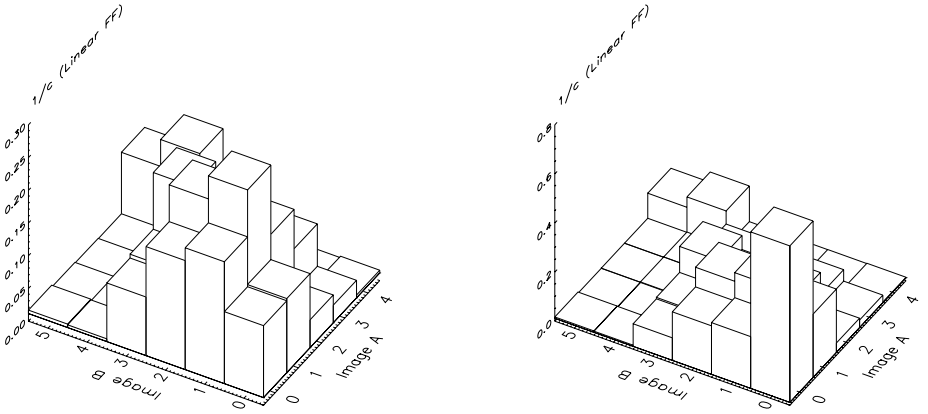

Figure 8 Loop association with linear force-free field model. The matrix $1/C_{L_A L_B}$(b), where C is in units of arcseconds, shows how well each loop in Image A associates with each loop in Image B. The horizontal axes are the loop numbers from Figure 4. Higher value corresponds to better association. The left panel shows the initial results of loop matching found by a coarse field line group. The right panel is the final results identified through the comparison with a more refined field line group. The maximum value of the vertical axis increases from 0.3 arcsec (left panel) to 0.8 arcsec (right panel).

Table 1 List of the possible loop pairs and α values of the field line best fitted with each loop pair.

Loop pair	Loop No. (Image A)	Loop No. (Image B)	$C_{L_A L_B}$(b) (arcsec)	αL
1	0	0	1.54	−1.2
2	1	1	3.08	−1.5
3	1	2	3.45	−1.5
4	2	3	4.63	−1.2
5	4	4	6.36	0.8

cannot be considered to represent a valid field model because their α value differs. We here use the field lines only as a means to associate loops. Wiegelmann and Neukirch (2002) also investigated whether the linear force-free field model is good enough to approximate the loops in active region NOAA 7986. They found similar results to this work: Different α values are needed to describe different subgroups of loops. So the nonlinear force-free field model would be a better field model for this active region (*cf.* Wiegelmann *et al.*, 2005b).

4.2. Complete Loop Feature Identification

One problem for the stereoscopy of loops is that the same segments of a loop are not always very visible and clearly identified in the two images. As can be seen from Figure 9, this is clearly the case for loop pair 1. We employ the best-fit magnetic field line b(0, 0) as a guide to extend the loops 0 in Images A and B. The originally identified loop and the field line b(0, 0) are overplotted on Image B in the left panels of Figure 10; the traced complete loop is shown in the right panels.

Lee, Newman, and Gary (2006) introduced a method to automatically segment solar loops based on the oriented connectivity and used the potential magnetic field model to guide the loop orientation. As they pointed out, sometimes the simplicity of the physical model

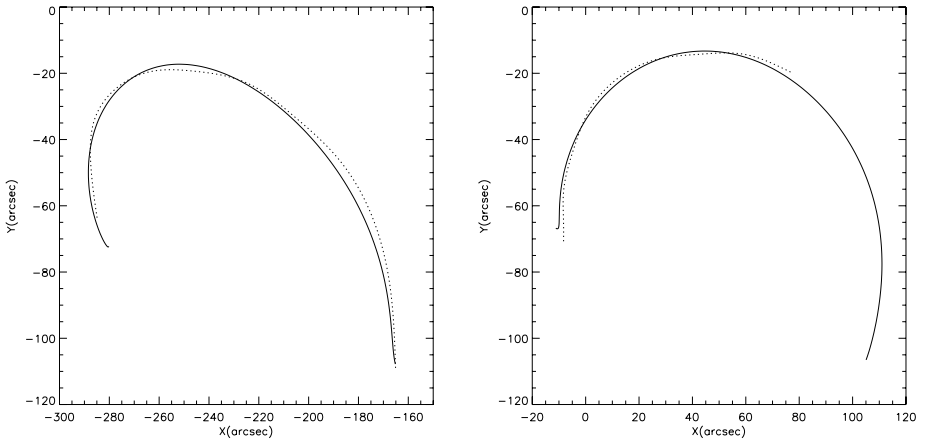

Figure 9 Dotted lines show loop No. 0 in Image A (left) and loop No. 0 in Image B (right); solid lines are projections of the best-fitting field line onto the respective image; we use b(0, 0) as the notation for this field line.

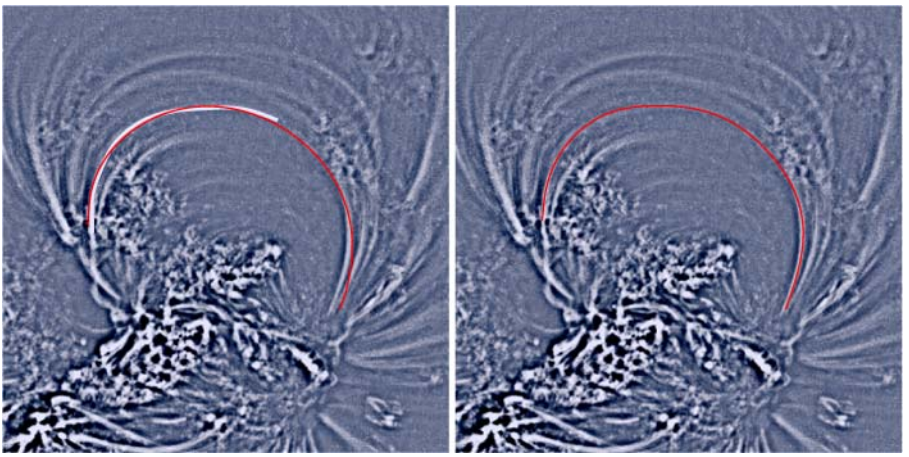

Figure 10 (Left) The white line shows the traced partial loop 0 in Image B and the red line is the best-fitting field line b(0, 0) with this loop. (Right) The red line shows the extended complete loop with the guide of the field line b(0, 0).

could cause the segmentation process to fail. Therefore, computed field lines lying as close as possible to the true loops should be combined to extract reliable loop structures. Without additional information it is hard to clearly identify loops in plasma images. A projection of computed magnetic field lines can help to achieve this aim. Magnetic field lines do, of course, exist in space, filling the corona, and might depend additionally on a priori unknown parameters (*e.g.*, the force-free parameter α). For the identification of a plasma loop we choose the field line (in 2D projection) closest to the loop in the image to guide the loop direction.

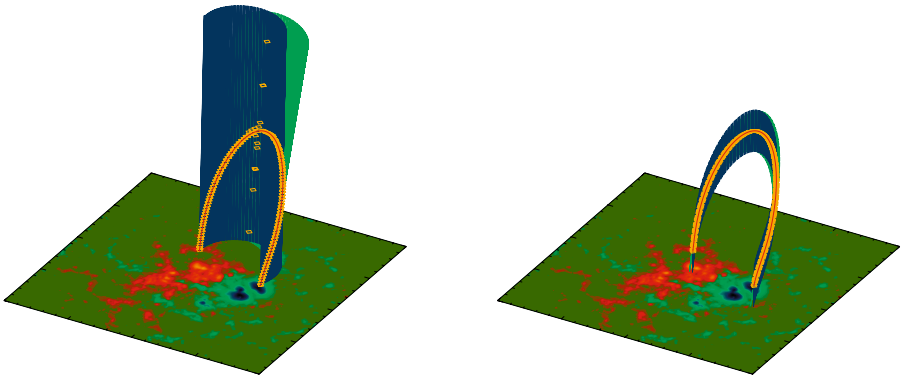

Figure 11 Geometrical stereoscopy from two projections of field line b(0, 0). The blue surface is generated by back projection along the view direction of Image A, and the green surface is along the view direction of Image B. Yellow points are the solutions of 3D reconstruction. (Left) The results of purely geometrical stereoscopy. (Right) The results of magnetic stereoscopy. The two red lines mark the 3D field line b(0, 0).

4.3. Stereoscopic Reconstruction

In this subsection we show as an example the stereoscopic reconstruction from the loop pair (0-0) and we demonstrate how the best-fitting field line b(0, 0) helps with this reconstruction.

For the stereoscopy method test, we at first reconstruct the 3D curve from the two projections of the field line b(0, 0) to check whether the result is the original 3D field line or not. The basic idea of our geometrical stereoscopy is given in the left panel of Figure 11. The 1D curves (projected field line or identified loop) can be projected back along the view direction, which generates a 3D solution surface on which the real 3D curve must lie. From two view directions, we obtain two such surfaces and their intersection must be the 3D solution (Wiegelmann *et al.*, 2005a; Wiegelmann and Inhester, 2006).

In the case of loop pair (0-0), classical stereoscopy gives two solutions: One is the correct original 3D field line; the other consists of some yellow points strung out nearly in the vertical direction. By considering the epipolar geometry, since the epipolar lines for STEREO and TRACE observation are only slightly inclined with respect to the ecliptic, loops in the north – south direction that intersect epipolar lines only once are reconstructed straight. For the loops in an east – west orientation, two-time intersection usually yields two solutions that cross each other (Inhester, 2006). Obviously the second solution is a ghost 3D feature introduced by the fact that the coronal plasma is optically thin and we should find a way to remove it. The presence of such ghosts is particularly annoying since most loops are expected to be oriented roughly in the east – west direction.

To get rid of the ghost feature we add the information of the best-fitting magnetic field line b(0, 0) to the purely geometrical stereoscopy. This is achieved by limiting the Z range (*i.e.*, normal coordinate) of the two back projection surfaces to ± 8 arcsec (the exact value is not important to the results) of Z values of the field line b(0, 0). The stereoscopic reconstruction result obtained by using this additional constraint is shown in the right panel of Figure 11. Now the ghost feature has disappeared.

Now we apply this magnetic stereoscopy method to the TRACE data, loop pair 0-0. The 3D reconstruction of this loop pair (Figure 12) is marked by the yellow dotted features, and the best-fitting 3D field line is marked by the red line. Generally, the yellow dotted features

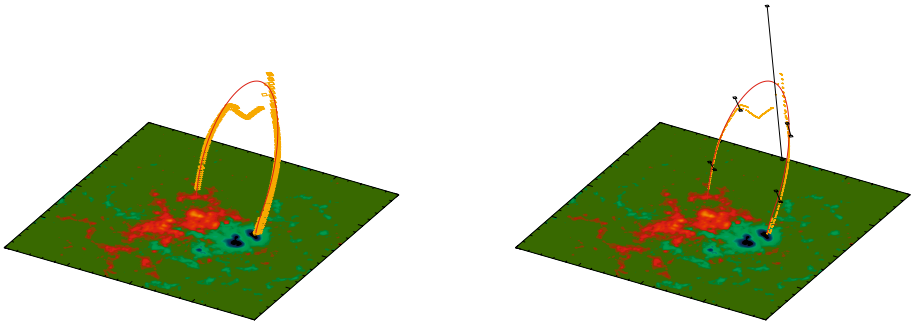

Figure 12 Magnetic stereoscopy of loop pair 0-0. Yellow points give the solution of the 3D reconstruction, the red line is the best-fitting 3D magnetic field line. The right panel shows the reconstruction error bars at five points along the 3D magnetic field line.

form a reasonable outline of the 3D loop except for the part near the loop top. As shown by Inhester (2006), the positional error of the 3D curve reconstruction can be estimated by $w/(2\sin(\gamma/2))$, where γ is the angle between the local projection surface normals and w is the width of the loop cross section in the EUV image. The difference in heliographic longitude of the spacecraft between the two days is about 17 degree. The angle γ cannot be larger than this stereo base angle. The two normal unit vectors of the projection surfaces become almost parallel near the loop top. Hence the loop top is the most difficult part to be reconstructed by stereoscopy. Our reconstruction lies within the error bars shown in the right panel of Figure 12. Since the two STEREO spacecraft will remain in the ecliptic the loop top will be the most uncertain part for any stereoscopic reconstruction of loops in the east – west orientation.

5. Conclusions

Wiegelmann and Inhester (2006) developed a tool for the stereoscopic reconstruction of plasma loops from two images taken from different viewpoints. In contrast to techniques developed earlier, This method makes full use of magnetic field extrapolation to help constrain the reconstructed loop. In this paper we have applied this tool to real data from TRACE and SOHO.

Two TRACE images of a long-lived active region recorded about one day apart can mimic two STEREO EUVI images from two different viewpoints owing to solar rotation. We identified 1D loop structures from two filtered images. In this work we performed the loop segmentation by hand, but we will employ an automated tool in the future. As shown earlier, a magnetic field line that is close to the loop structure could be a useful guide to trace a complete loop and find the position of the loop footpoints.

The magnetic field in the solar corona is extrapolated with the linear force-free field model from line-of-sight MDI magnetograms. The extrapolated 3D field lines are then projected onto two TRACE images to associate the loops in one image with the loops in the other image. In total, we found five possible loop pairs with different linear force-free α values related to them. However, because of some temporal evolution of coronal loops during the two days it is difficult to confirm that they are indeed the same loop seen from two different vantage points. The different α values for different loop pairs indicate that a linear force-free field model is not appropriate for the coronal loops in active region NOAA 8891.

We reconstruct the 3D loop structure for the most probable loop pair. We demonstrate that the magnetic stereoscopy tool can remove the ambiguities from the classical geometrical stereoscopy. The results of magnetic stereoscopy reproduce the 3D loop structure well except at the loop top, which is the most difficult part to reconstruct, but even that part is significantly constrained by the best-fitting field line.

We expect that better stereoscopic results can be obtained with simultaneous STEREO data, with an automated loop segmentation tool, and with a better magnetic field model such as a nonlinear force-free field. The computation of nonlinear force-free fields is mathematically more challenging because of the nonlinearity of the mathematical task and in addition these models require vector magnetograms as input. Several methods have been developed to compute nonlinear force-free fields; see, *e.g.*, Sakurai (1981), Schrijver *et al.* (2006), Valori, Kliem, and Keppens (2005), and Wiegelmann (2004). The ground-based full-disk vector magnetograph Synoptic Optical Long-term Investigations of the Sun (SOLIS) and the Solar Optical Telescope (SOT) on *Hinode* (*Solar B*), launched in September 2006, will provide us with vector magnetograms. As pointed out by Wiegelmann and Inhester (2006), the stereoscopic reconstructed plasma loops might be used to improve the coronal magnetic field model.

Acknowledgements The authors thank the SOHO/MDI, EIT, and TRACE consortia for their data. SOHO is a joint project of ESA and NASA. We thank Markus Aschwanden for useful discussions. The work of L. Feng was supported by the International Max-Planck Research School on Physical Processes in the Solar System and Beyond at the Universities of Braunschweig and Goettingen. The work of T. Wiegelmann was supported by DLR Grant No. 500C 0501 and the work of W.Q. Gan was supported by a grant numbered as 2006CB806300.

Appendix

To project the 3D field lines onto two TRACE images we define three different coordinate systems. For a detailed introduction to the coordinate systems for solar images see Thompson (2006).

- *Heliographic coordinate* (*HGC*) *system*: The heliographic coordinate system is corotating with the solar surface. It is independent of the positions of the spacecraft. A position on the solar surface is generally specified by heliographic longitude and latitude coordinates (L, B) (in units of degrees). The position of the observer is usually localized in this coordinate system and can be found in the FITS header OBS_B0, $0BS\_L0$. The z axis of this HGC system is along the solar rotation axis; the x and y axes are in the heliographic equator plane toward 0° and 90° Carrington longitude, respectively. Numerical coordinate values are conveniently given in units of solar radius.
- *Heliocentric coordinate* (*HCC*) *system*: The coordinates of TRACE and EIT observation are in heliocentric coordinate systems, which are related to the spacecraft positions. This coordinate system has its origin at the solar center. The z axis points to the observer, the x axis is along the cross product of the z axes of the heliographic and heliocentric coordinate systems, and the y axis is the cross product of the z axis and x axis to make the system right handed. As mentioned earlier TRACE images are aligned with EIT data, which have been mapped to the earth view; the position of viewpoint in the heliographic coordinate system then is given by the $EARTH\_B0$ and $EARTH\_L0$ in the FITS header of EIT data.

  For an observing point (L, B) in the heliographic system, we can calculate the unit vectors along three axes of the corresponding heliocentric coordinate system. They are

stored in the three columns of matrix A:

$$\begin{pmatrix} -\sin L & -\cos L \sin B & \cos L \cos B \\ \cos L & -\sin L \sin B & \sin L \cos B \\ 0 & \cos B & \sin B \end{pmatrix}.$$

Given a vector $\mathbf{r}_{\rm HGC}$ represented by the three HGC coordinates, the projection along three unit vectors of HCC gives the coordinates of $\mathbf{r}_{\rm HGC}$ in the heliocentric coordinate system $\mathbf{r}_{\rm HCC}$. Therefore, the transformation from $\mathbf{r}_{\rm HGC}$ to $\mathbf{r}_{\rm HCC}$ can be expressed as

$$\mathbf{r}_{\rm HCC} = A^{\rm T}\mathbf{r}_{\rm HGC}. \tag{4}$$

Conversely,

$$\mathbf{r}_{\rm HGC} = A\mathbf{r}_{\rm HCC}. \tag{5}$$

With these two expressions we can transform between the heliocentric coordinate systems for two TRACE (EIT earth) viewpoints.

– *Magnetic field extrapolation coordinate* (*MEC*) *system*: To project the 3D field lines onto two TRACE images we should convert the coordinates in the MEC system to the coordinates in the two HCC systems for two TRACE observations. The idea is that we first transform the MEC system to the HGC system and then to the two TRACE HCC systems separately by Equation (4).

The Seehafer method of linear force-free field extrapolation is computed on a rectangular grid ($0-L_x$ and $0-L_y$), covering the area chosen in the MDI data (see Figure 1). For convenience of transformation, we shift the origin of this coordinate system to the center of the selected region ($\frac{1}{2}L_x$, $\frac{1}{2}L_y$) on the solar surface. The z axis points outward from the coordinate origin along the connection line of the solar center and the shifted origin; the x and y axes lie in the plane vertical to the z axis. This MEC system is easily transformed to the HCC system by shifting the origin from the solar surface to the solar center and rescaling to the units of solar radius, as the numerical coordinate values in this extrapolation coordinate system are given in units of MDI pixels.

To transform the coordinates in the HCC system to the HGC system we should know the coordinate values (L, B) of the origin in the heliographic coordinate system. To find them we calculate its heliocentric coordinate values in units of arcseconds first from the pixel system by

$$x = \mathrm{CDELT1}(i - \mathrm{CRPIX1}), \tag{6}$$

$$y = \mathrm{CDELT2}(j - \mathrm{CRPIX2}), \tag{7}$$

$$z = \sqrt{R_\odot^2 - x^2 - y^2}. \tag{8}$$

Here (i, j) are the coordinates of the origin in the pixel system and (x, y, z) are the coordinates in the heliocentric coordinate system. CDELT1, CDELT2, CRPIX1, and CRPIX2 can be found in the FITS header of MDI data and give the spatial resolution in units of arcseconds and the position of Sun center in the pixel system. The (x, y, z) values in units of arcseconds can be easily converted to the values in units of solar radius. Now the coordinate values of the origin can be transformed to the heliographic coordinates according to Equation (5) to get the (L, B) coordinates of the origin.

With the (L, B) values of the origin the coordinates of the 3D field lines in the HCC system can now be converted to the coordinates in the HGC system. The whole process

from the MEC system to the HGC system is shown by the following equation:

$$\mathbf{r}_{\mathrm{HGC}} = A_{\mathrm{MEC}}\left[\frac{\mathbf{r}_{\mathrm{MEC}} - (\frac{1}{2}L_x, \frac{1}{2}L_y, 0)^{\mathrm{T}}}{R_{\odot}(\mathrm{pixel})} + (0, 0, 1)^{\mathrm{T}}\right]. \tag{9}$$

Then the coordinates in the TRACE HCC system can be calculated with Equation (10) by applying Equation (4), where A_{MEC} has the (L, B) coordinates of the origin of the MEC system and A_{TRACE} that of the TRACE spacecraft position:

$$\mathbf{r}_{\mathrm{HCC}} = A^{\mathrm{T}}_{\mathrm{TRACE}}\mathbf{r}_{\mathrm{HGC}} = A^{\mathrm{T}}_{\mathrm{TRACE}}A_{\mathrm{MEC}}\left[\frac{\mathbf{r}_{\mathrm{MEC}} - (\frac{1}{2}L_x, \frac{1}{2}L_y, 0)^{\mathrm{T}}}{R_{\odot}(\mathrm{pixel})} + (0, 0, 1)^{T}\right]. \tag{10}$$

For the projections onto the TRACE images, only x and y values are needed.

References

Aschwanden, M.J.: 2005, *Solar Phys.* **228**, 339.
Aschwanden, M.J., Nightingale, R.W.: 2005, *Astrophys. J.* **633**, 499.
Aschwanden, M.J., Newmark, J.S., Delaboudinière, J.-P., Neupert, W.M., Klimchuk, J.A., Gary, G.A., *et al.*: 1999, *Astrophys. J.* **515**, 842.
Aschwanden, M.J., Alexander, D., Hurlburt, N., Newmark, J.S., Neupert, W.M., Klimchuk, J.A., *et al.*: 2000, *Astrophys. J.* **531**, 1129.
Berton, R., Sakurai, T.: 1985, *Solar Phys.* **96**, 93.
Carcedo, L., Brown, D.S., Hood, A.W., Neukirch, T., Wiegelmann, T.: 2003, *Solar Phys.* **218**, 29.
Delaboudiniere, J.-P., Artzner, G.E., Brunaud, J., Gabriel, A.H., Hochedez, J.F., Millier, F., *et al.*: 1995, *Solar Phys.* **162**, 291.
Handy, B.N., Acton, L.W., Kankelborg, C.C., Wolfson, C.J., Akin, D.J., Bruner, M.E., *et al.*: 1999, *Solar Phys.* **187**, 229.
Inhester, B.: 2006, arXiv: astro-ph/0612649v1.
Lee, J.K., Newman, T.S., Gary, G.A.: 2006, *Pattern Recognit.* **39**, 246.
Marsch, E., Wiegelmann, T., Xia, L.D.: 2004, *Astron. Astrophys.* **428**, 629.
Portier-Fozzani, F., Inhester, B.: 2001, *Space Sci. Rev.* **97**, 51.
Sakurai, T.: 1981, *Solar Phys.* **69**, 343.
Scherrer, P.H., Bogart, R.S., Bush, R.I., Hoeksema, J.T., Kosovichev, A.G., Schou, J., *et al.*: 1995, *Solar Phys.* **162**, 129.
Schrijver, C.J., DeRosa, M.L., Metcalf, T.R., Liu, Y., McTiernan, J., Regnier, J., *et al.*: 2006, *Solar Phys.* **235**, 261.
Seehafer, N.: 1978, *Solar Phys.* **58**, 215.
Solanki, S.K.: 1993, *Space Sci. Rev.* **63**, 1.
Thompson, W.T.: 2006, *Astron. Astrophys.* **449**, 791.
Valori, G., Kliem, B., Keppens, R.: 2005, *Astron. Astrophys.* **433**, 335.
Wiegelmann, T.: 2004, *Solar Phys.* **219**, 87.
Wiegelmann, T., Inhester, B.: 2006, *Solar Phys.* **236**, 25.
Wiegelmann, T., Neukirch, T.: 2002, *Solar Phys.* **208**, 233.
Wiegelmann, T., Inhester, B., Sakurai, T.: 2006, *Solar Phys.* **233**, 215.
Wiegelmann, T., Inhester, B., Lagg, A., Solanki, S.K.: 2005a, *Solar Phys.* **228**, 67.
Wiegelmann, T., Lagg, A., Solanki, S.K., Inhester, B., Woch, J.: 2005b, *Astron. Astrophys.* **433**, 701.